

Reversal of Orbital Hall Conductivity and Emergence of Tunable Topological Quantum States in Orbital Hall Insulator

Shilei Ji,¹ Chuye Quan,¹ Ruijia Yao,¹ Jianping Yang,² and Xing'ao Li^{1,2,3,*}

¹*Institute of Advanced Materials (IAM), Nanjing University of Posts and Telecommunications (NJUPT), Nanjing 210023, China.*

²*School of Science, Jiangsu Provincial Engineering Research Center of Low Dimensional Physics and New Energy, Nanjing University of Posts and Telecommunications (NJUPT), Nanjing 210023, China.*

³*College of science, Zhejiang University of Science and Technology, Hangzhou 310023, China.*

(Dated: February 23, 2024)

Recent findings indicate that orbital angular momentum (OAM) has the capability to induce the intrinsic orbital Hall effect (OHE), which is characterized by orbital Chern number in the orbital Hall insulator. Unlike the spin-polarized channel in Quantum anomalous Hall insulator, the OAM is valley-locked, posing challenges in manipulating the corresponding edge state. Here we demonstrate the sign-reversal orbital Chern number through strain engineering by combing the $k \cdot p$ model and first-principles calculation. Under the manipulation of strain, we observe the transfer of non-zero OAM from the valence band to the conduction band, aligning with the orbital contribution in the electronic structure. Our investigation reveals that electrons and holes with OAM exhibit opposing trajectories, resulting in a reversal of the orbital Hall conductivity. Furthermore, we explore the topological quantum state between the sign-reversible OHE.

I. INTRODUCTION

The orbital Hall effect (OHE) occurs in response to a transverse electric field, wherein carriers with orbital angular momentum (OAM) undergo longitudinal displacement, leading to an observable electrical response.[1–5] It is regarded as the orbital analog of the spin Hall effect (SHE).[6–10] However, unlike SHE, the OHE can be observed in materials with weak spin-orbit coupling (SOC).[1, 11, 12] In contrast to the spin and anomalous Hall effects, directly detecting the accumulation of OAM faces inherent limitations, restricting the advancement of the OHE. Recent developments in experiments have revealed pronounced OHE in light metals, with validation achieved through the magneto-optical Kerr effect (MOKE).[1] This discovery not only underscores the challenges associated with probing OAM but also marks a pivotal milestone in exploring the OHE and its topological properties.

OAM[9, 13–15], referred to as orbital magnetic moment[7, 8, 16–19] or orbital texture[4, 20, 21], plays a pivotal role as the source of the OHE—an observation substantiated through both experimental and theoretical avenues. In two-dimensional (2D) transition metal dichalcogenides (TMDs), the presence of non-zero OAM with opposite signs in two valleys, under the protection of C_3 symmetry, gives rise to a topologically protected OHE.[7, 13, 20, 22, 23] This intriguing behavior is expressed through the topological invariant known as the orbital Chern number (C_L). Remarkably, carriers excited in the K valley exhibit positive OAM, moving in the opposite direction to those in the K' valley carrying negative OAM.[3, 13, 24, 25] The unique electronic motion gives

rise to topologically protected quantum states, reminiscent of the purely spin-polarized currents observed in the quantum spin Hall effect.[26, 27]

Furthermore, within TMDs, there exist other topological quantum states, such as the quantum anomalous Hall Effect (QAHE), which manifests specifically in ferromagnetic systems.[28–34] A single spin-polarized electronic structure near the Fermi level leads to spin-polarized edge states in QAHE. Changing the magnetic moment direction in TMDs can induce a reversal of the conductive channel at the edge.[31] However, in the context of OHE, the OAM is valley-locked, making it impossible for carriers excited in the K valley to carry negative OAM.[7, 16, 20, 25, 35] Modifying the C_L by manipulating OAM in the valley is thus deemed unfeasible. The following issue arises: can the edge states of OHE be manipulated, and is it possible to alter the direction of motion for carriers with OAM?

Here we close this gap by using a strain engineering to investigate the interplay between the OAM and C_L . Combining the $k \cdot p$ model with first-principles calculations, we show that non-zero OAM patterns can switch between the valence and conduction bands under strain. With the application of strain, the band gap within the valley undergoes a gradual closure and subsequent reopening. Concurrently, the orbital contributions on the valence band shift from magnetic quantum numbers ± 2 to 0. We prove that there are three different topological quantum states in this process, corresponding to OHE, QAHE, and OHE respectively, and their C_L of +1, 0, and -1 . Subsequently, we explore the transport behavior under various C_L . It becomes evident that the OAM patterns in both the valence and conduction bands dictate the types of charge carriers with non-zero OAM, thereby leading to the different topological phase transitions.

* lxahbmy@126.com

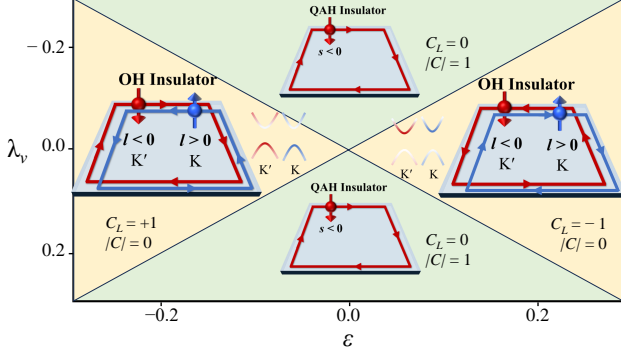


FIG. 1. The schematic diagrams of topological quantum state calculated by two band $k \cdot p$ model. The other parameters are set as $\Delta = 0$ eV, $v_F = 1$ eV, and $D = 1$ eV. s and l are the spin and orbital angular momentum, respectively. The non-zero orbital Chern number C_L and Chern number C represent the orbital Hall (OH) insulator and quantum anomalous Hall (QAH) insulator. With the gradual increase in the parameter ε , the system sequentially transitions through phases of OH insulator, QAH insulator, and back to OH insulator, corresponding to C_L of $+1$, 0 , and -1 , respectively. We depict the Orbital Angular Momentum (OAM) in the OH insulator, where the colors blue and red represent $\pm 2\hbar$.

II. TWO BAND $k \cdot p$ ANALYSIS

Traditional TMD monolayers, such as H-VSe₂, [34, 36–39] breaking the spatial and time reversal symmetry, have been demonstrated to be an ideal platform to investigate OHE. The unique and clean valley model at K and K' points has a non-zero valley Chern number at the basis of $\psi_v^\tau = (|d_{x^2-y^2}\rangle + i\tau|d_{xy}\rangle)/\sqrt{2}$ and $\psi_c^\tau = |d_{z^2}\rangle$, where the index $\tau = +1$ (-1) represents the K (K') valley, and v/c denotes the valence/conduction state. The corresponding effective Hamiltonian H_{eff} can be written as below, [40–43]

$$H_{\text{eff}} = v_F(\tau\hat{\sigma}_x k_x + \hat{\sigma}_y k_y) + \frac{\Delta}{2}\hat{\sigma}_z - \tau\hat{s}_z\lambda_v\frac{\hat{\sigma}_z - 1}{2}. \quad (1)$$

Here, v_F is the massless Fermi velocity of the Dirac electrons, $\hat{\sigma}_i$ and \hat{s}_i ($i = 0, x, y, z$) are Pauli matrices for pseudospin and spin, respectively. In addition, the band gap of the system is represented by Δ , and λ_v is the SOC parameter for the valence band. The interface engineering is an effective method to manipulate the electrical properties of TMDs. [28, 29, 31, 34, 44–47] In our $k \cdot p$ model, an additional term H_ε has been added to Eq. 1,

$$H_\varepsilon = -\frac{D}{2}\varepsilon\hat{s}_0\hat{\sigma}_z \quad (2)$$

which can apply a biaxial in-plane strain $\varepsilon = (a - a_0)/a_0$ to TMD. Where a and a_0 denote strained and equilibrium lattice constants, and D is the deformation potential.

The spin channels at the top of the valence band for two valleys are spin-up. The spin index is $+1$, and the Hamiltonian eigenvalues are expressed as: $E_\pm =$

$\frac{1}{2}[\tau\lambda_v \pm \sqrt{4v_F^2 k^2 + (\Delta_\tau - D\varepsilon)^2}]$, where $\Delta_\tau = \Delta - \tau\lambda_v$. In addition, k^2 is equal to $k_x^2 + k_y^2$. The Berry curvature (BC) $\Omega_n^{\tau,z}(\mathbf{k})$ and orbital Berry curvature (OBC) $\Omega_n^{\tau,\hat{L}_z}(\mathbf{k})$ at the valley can be written as

$$\begin{aligned} \Omega_n^{\tau,z}(\mathbf{k}) &= -2\hbar^2 \sum_{n \neq n'} \frac{\text{Im}\langle\psi_{n\mathbf{k}}|\hat{v}_x|\psi_{n'\mathbf{k}}\rangle\langle\psi_{n'\mathbf{k}}|\hat{v}_y|\psi_{n\mathbf{k}}\rangle}{(E_{n'} - E_n)^2} \\ \Omega_n^{\tau,\hat{L}_z}(\mathbf{k}) &= -2\hbar \sum_{n \neq n'} \frac{\text{Im}\langle\psi_{n\mathbf{k}}|\hat{v}_x|\psi_{n'\mathbf{k}}\rangle\langle\psi_{n'\mathbf{k}}|\hat{J}_y|\psi_{n\mathbf{k}}\rangle}{(E_{n'} - E_n)^2} \end{aligned} \quad (3)$$

Where \hat{v}_i ($i = x, y$) is the velocity operator along the k_i direction and the OAM operator \hat{J}_y is defined as $\hat{J}_y = \frac{1}{2}(\hat{v}_y\hat{L}_z + \hat{L}_z\hat{v}_y)$. \hat{L}_z is the z components of the OAM operator. In the $k \cdot p$ model, there are two different descriptions to represent the OAM operator: the Bloch state orbital magnetic moment \hat{L}_z^{tot} [13, 16, 17, 25] and the intra-atomic approximation \hat{L}_z^{intra} [3, 4, 6, 7, 11]. Here, we focus on the second description: the intra-atomic approximation, where the source of the orbital magnetic moment neglected the intersite circulation current, which has been demonstrated to be effective and accurate in the study of OHE. [3, 4, 6, 7, 11] Based on the basis function of ψ_c^τ and ψ_v^τ defined above, the OAM operator can be chosen as $\hat{L}_z = \text{diag}(0, 2\hbar\tau)$ for analytical solution of OHE. The BC and OBC at special valley can be simplified as

$$\begin{aligned} \Omega_n^{\tau,z}(\mathbf{k}) &= \tau \times \Omega_n^{\tau,\hat{L}_z}(\mathbf{k}) \\ &= \frac{2\tau v_F^2 (\Delta_\tau - D\varepsilon)}{(4v_F^2 k^2 + (\Delta_\tau - D\varepsilon)^2)^{3/2}} \end{aligned} \quad (4)$$

The values of BC and OBC are closely related to the band gaps and have extreme values on the two valleys. It is interesting that, the symbol of OBC on K' ($\tau = -1$) valley is the opposite of BC, while it is the same on K ($\tau = 1$) valley. This means that, when integrating BC and OBC near the K' valley, the corresponding Chern numbers are negative to each other. The quantum anomalous Hall (QAH) insulator has a chiral, non-dissipative spin channel at the edge of the bulk state, which has an integer multiple of Chern number. In our description, the Chern number can be written as $C = \frac{1}{2} \sum_\tau \tau \times \text{sgn}(\Delta_\tau - D\varepsilon)$. In addition, the orbital Hall (OH) insulator is a topological insulator whose currents across two valleys carry opposite OAM. The orbital Chern number $C_{\hat{L}_z} = \frac{1}{2} \sum_\tau \tau \text{sgn}(\Delta_\tau - D\varepsilon)$ is a topological invariant to characterize OH insulators.

We plot a topological quantum diagram of the SOC parameter λ_v as a function of biaxial strain ε in Fig. 1. For a system without considering λ_v and ε , both valleys simultaneously close, exhibiting a topologically trivial state. The application of strain can open the band gap, giving rise to the OHE with a topological invariant $C_L = \pm 1$. This indicates that the generation of OHE does not require SOC, aligning with the conclusions of previous studies. [1, 4, 20] Subsequently, when

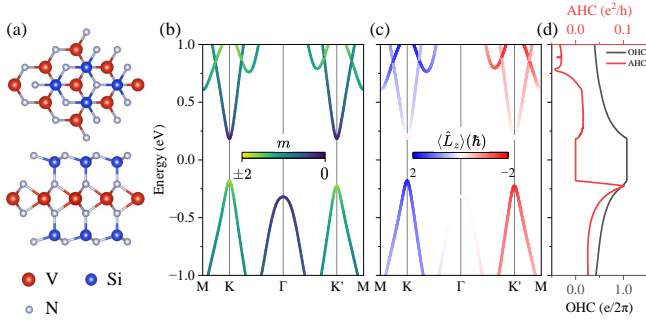


FIG. 2. The first-principle calculations of 1L VSi₂N₄. (a) The atomic structure of 1L VSi₂N₄. Up and down panels are the top and side view, respectively. (b) The electronic and (c) orbital band structure for 1L VSi₂N₄, where m and $\langle \hat{L}_z \rangle$ represent the magnetic quantum number and orbital angular momentum. Here, $m = \pm 2$ is used to represent the d_{xy} and $d_{x^2-y^2}$ orbitals, while $m = 0$ is employed to signify the d_{z^2} orbital. The anomalous Hall conductivity and orbital Hall conductivity are plotted in (d), which are represented by red and black lines, respectively.

$\lambda_v \neq 0$ without strain, the system is a QAH insulator with $|C| = 1$. When $|\varepsilon| > |\lambda_v|$, the system transitions from QAHE to OHE with valley polarization. This corresponds to a topological index $C_L = \pm 1$. Interestingly, for $\varepsilon < 0$, $C_L = +1$, while for $\varepsilon > 0$, $C_L = -1$. These two types of OHE with opposite topological indices are intriguingly associated with the sign of ε . To investigate the change in C_L , we calculate the OAM in the valley,

$$\langle \hat{L}_{z,\mathbf{k}} \rangle = \langle \psi_{\mathbf{k}} | \hat{L}_{z,\mathbf{k}} | \psi_{\mathbf{k}} \rangle. \quad (5)$$

The expectation values of OAM in both valleys are $\pm 2\hbar$. Notably, under the condition of $\varepsilon < 0$, $\langle \hat{L}_z \rangle = \pm 2\hbar$ occurs at the top of the valence band, while for $\varepsilon > 0$, it is observed at the bottom of the conduction band. This observation suggests that, while maintaining a constant OAM, strain engineering has the capability to manipulate the edge states of electrons and holes in OH insulators. The C_L emerges as an effective descriptor delineating these distinct edge states.

III. DFT-BASED CALCULATIONS

A. OHE and OAM for VSi₂N₄

To realize the tunable topological quantum states, we propose a family of OH insulator, VA₂Z₄ (A = Si, Ge; Z = N, P, As) in Fig. 2(a). [28, 32, 34, 44] Which has been extensively employed in the investigation of both the QAHE and the Valley Hall Effect. Note that, despite VSi₂N₄ is not a TMD (MX₂), in a stoichiometric sense, it is ruled by a similar low-energy theory. In this work, taking VSi₂N₄ as an example, we investigate the strain-dependent topological phase transition. The electronic

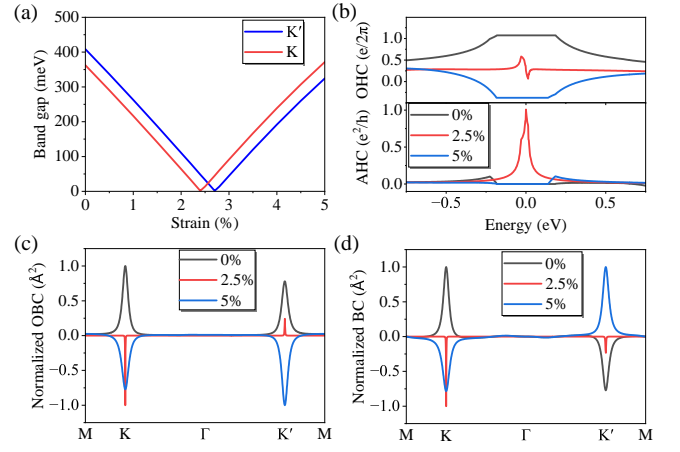


FIG. 3. The transport property of 1L VSi₂N₄ with the first-principle calculations combining Wannier function. (a) The band gaps at two valleys as a function of strain. The Blue and red lines are the K and K' valleys. There is a band reversal near the strain of 2.5%. We choose 0% (black line), 2.5% (red line), and 5% strain (blue line) as three different cases to investigate the topological quantum state. The corresponding orbital Hall conductivity (OHC) and anomalous Hall conductivity (AHC) are plotted in (b). In addition, we analysis (c) the Normalized orbital Berry curvature and (d) Berry curvature through the first Brillouin Zone.

structure plotted in Fig. 2(b) is a direct gap semiconductor with the shape of valley. Due to the non-negligible SOC in transition metals, the valley splitting of VSi₂N₄ at the two valleys occurs in the valence band occupied by d_{xy} and $d_{x^2-y^2}$. In addition, in Fig. 2(c), we display the OAM-resolved band structure by calculating the expectation value of \hat{L}_z . By comparing the results of $k \cdot p$ model and DFT, we find that non-zero magnetic quantum numbers (d_{xy} and $d_{x^2-y^2}$) can produce large OAMs at two valleys. At two valleys, the expectation value $\langle \hat{L}_z \rangle$ can reaches $\sim \pm 2\hbar$. When an in-plane electric field is applied to VSi₂N₄, the carriers generated in the valley carry not only the spin angular momentum but also the OAM, which is AHE and OHE, respectively. For a 2D system, the anomalous Hall conductivity σ_{xy}^{AH} and orbital Hall conductivity σ_{xy}^{OH} can be calculated by

$$\begin{aligned} \sigma_{xy}^{AH} &= -\frac{e^2}{\hbar} \sum_n \int_{BZ} \frac{d^2k}{(2\pi)^2} f_{n\mathbf{k}} \Omega_n^z(\mathbf{k}) \\ \sigma_{xy}^{OH} &= \frac{e}{\hbar} \sum_n \int_{BZ} \frac{d^2k}{(2\pi)^2} f_{n\mathbf{k}} \Omega_n^{\hat{L}_z}(\mathbf{k}). \end{aligned} \quad (6)$$

Here, $\Omega_n^z(\mathbf{k})$ and $\Omega_n^{\hat{L}_z}(\mathbf{k})$ are Berry curvature and orbital Berry curvature, respectively. Moreover, BZ represents the Brillouin zone and $f_{n\mathbf{k}}$ is the Fermi-Dirac distribution. The Fig. 2(d) shows the AHE and OHE of VSi₂N₄. Within the band gap, the anomalous Hall conductivity (AHC) vanishes while the orbital Hall conductivity (OHC) occurs with the value of $1.1 e/2\pi$. Combining

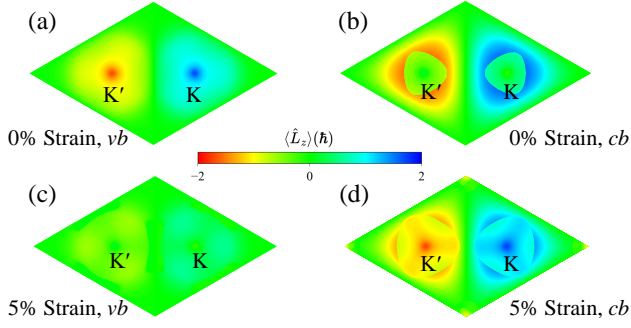


FIG. 4. The orbital angular momentum (OAM) distribution of (a) valance band (vb) at 0% strain, (b) conduction band (cb) at 0% strain, (c) vb at 5% strain, and (d) cb at 5% strain. The blue/red dot represents $\langle \hat{L}_z \rangle = +2/-2\hbar$. The OAM distribution of 1L VSi_2N_4 is calculated by the first-principle calculations combining Wannier function.

with $k \cdot p$ analysis, we observe $C = 0$ while $C_{\hat{L}_z} = +1$, indicating that VSi_2N_4 is an OH insulator. The giant OHC arises from $d_{xy} + d_{x^2-y^2}$ orbitals and non-zero OAM.

B. Interface engineering

Interface engineering, such as strain, is an effective method for tuning the electronic and orbital structures of 2D materials. In order to manipulate the topological quantum states in VSi_2N_4 , we apply biaxial strain to it without altering the spatial symmetry in Fig. 3(a). In the first-principle calculations, the biaxial strain can be applied by changing the lattice constant with the equation $\varepsilon = (a - a_0)/a_0$, where a and a_0 are the strained and equilibrium lattice constant. We observe a linear trend in the change of band gap with strain, consistent with the conclusion drawn in Fig. 1. (see details on electronic structures and fitting results in the Supplemental Material[48]) When the strain reaches 2.4%, the band on K point closes, and it reopens as the strain further increases. At this point, there is a band inversion, with the conduction band contributed by d_{xy} and $d_{x^2-y^2}$ orbitals, while the valence band is contributed by d_{z^2} orbital. When the strain reaches 2.7%, a similar transition occurs in the K' valley.

According to the $k \cdot p$ model, we categorize VSi_2N_4 under strain into three cases, corresponding to OH, QAH, and OH insulators as outlined in Fig. 1. The detailed orbital contribution can be obtained in the Supplemental Material[48]. Subsequently, we calculate the AHE and OHE for the three cases in Fig. 3(b). A significant OHC accompanying $C_L = \pm 1$ is observed when the strain is 0% and 5%. Since there are not only two bands contributing near the Fermi level, OHCs are not equal to zero in all three cases. In particular, the OHC is about $-0.4 e/2\pi$ for the 5% strain, which is mainly because the $k \cdot p$ model can only describe the situation near the

Fermi level and cannot characterize the electrical properties on all energy levels. As supported by the Fig. S4 in the Supplemental Material[48], as the number of energy levels considered in OHC calculation increases, the value of OHC tends to converge. We find that the contribution of OHC in the band gap is still dominated by the two valleys, similar to the case in OBC in Fig. 3(c). By fitting the first-principles calculation with $k \cdot p$ model, we confirm that, 1L VSi_2N_4 is an OH insulator with the $C_L = -1$ at the strain of 5%. Moreover, at 2.5% strain, VSi_2N_4 becomes a QAH insulator with $|C| = 1$. Tensile strain induces changes in the band structure, leading to alterations in the topological quantum states. Figs. 3(b) and (c) illustrate the BC and OBC. In the strain of 0% and 5%, the sign of the BC is opposite in the two valleys, leading to the disappearance of AHE. The OBC, on the other hand, exhibits a different behavior. In both cases, the OBC has the same sign, indicating that carriers with opposite OAM in the two valleys have opposite trajectories, resulting in a non-zero C_L . At this point, VSi_2N_4 becomes an OH insulator. When the case switches to 2.5% strain, the conclusions are reversed compared to the above. Therefore, under the modulation of a strain field, VSi_2N_4 exhibits rich electronic properties and topological quantum states.

C. OAM for different topological quantum states

Although VSi_2N_4 returns to OHE under strain, it is interesting to note that the topological index is not the same as that without strain. As we can see from Fig. 3(b), the strain changes the direction of movement of the carriers in two valleys, resulting in OHC with opposite signs. The different orbital Chern numbers, namely -1 and $+1$, are observed. Interestingly, the OAM in the $k \cdot p$ model is locked to the valley ($\langle \hat{L}_z^\tau \rangle = 2\hbar\tau$). This means that the OAM of VSi_2N_4 under strain does not change. However, the C_L shifts from $+1$ to -1 , indicating a reversal in the direction of motion for carriers carrying OAM. To understand the underlying principles, we investigate the OAM among different quantum states. Detailed OAM for the valence band and conduction band is depicted in Fig. 4. In the absence of strain, the OAM on the valence band is $\sim \pm 2\hbar$, while the OAM near the conduction band valley is approximately $0\hbar$. When applying an electric field, the motion of holes on VSi_2N_4 is topologically protected due to the non-zero OAM. Subsequently, we shift our focus to a 5% strain, where there is a reversal in the orbital contributions of the valence and conduction bands. This results in $\langle \hat{L}_z^{vb} \rangle \sim 0\hbar$ in the valence band and $\langle \hat{L}_z^{cb} \rangle \sim \pm 2\hbar$ in the conduction band near the valley. The electrons excited in OH insulator carry OAM of $\pm 2\hbar$ in opposite directions compared to 0%, and this process is topologically protected. In both cases, the different transport modes of electrons and holes carrying OAM lead to a shift in the C_L from $+1$ to -1 . In addition, we summarize the OAM patterns of three

cases in Fig. S3 in the Supplemental Material[48]. We observed distinct OAM patterns for different quantum states. Under strain engineering, the unique OAM patterns serve as a distinguishing feature for discerning the topological quantum states. Currently, directly detecting current with OAM in experiments remains challenging. Our work provides a novel perspective for exploring OHE.

IV. CONCLUSION

In summary, we have established the connection between the OHE and OAM for 2D TMDs. The types of carriers with non-zero OAM can effectively influence the C_L of OH insulators. Additionally, based on the band inversion under strain, we propose an effective method to manipulate the OAM and C_L of the system. Taking VSi_2N_4 as an example, we demonstrate the changes in AHC and OHC under strain and observe topological phase transitions from OHE to QAHE to OHE. However, applying tensile strain does not revert VSi_2N_4 to its initial topological state, as the C_L becomes opposite to that without strain. The OAM patterns in the valence

and conduction bands reveal that $\langle \hat{L}_z \rangle = \pm 2\hbar$ transitions from the valence to the conduction bands. The different OAM patterns can give us a new perspective to understand and manipulate the OH insulator. In experiments, the detection and verification of intrinsic OHC and its topological invariant still face great challenges. Our work shows that distinct OAM patterns can produce different topological quantum states. Therefore, for TMDs materials, we propose such an idea to solve the above problems. By employing optical and electrical methods to detect the OAM patterns on the valleys of valence and conduction bands, we can definitively confirm the presence of the OH insulator.

ACKNOWLEDGMENTS

We acknowledge the fundings from National Natural Science Foundation of China (Grant No. 51872145), and Postgraduate Research & Practice Innovation Program of Jiangsu Province (Grant No. KYCX20-0748, KYCX19-0935, KYCX23-0977).

-
- [1] Y. G. Choi, D. Jo, K. H. Ko, D. Go, K. H. Kim, H. G. Park, C. Kim, B. C. Min, G. M. Choi, and H. W. Lee, Observation of the orbital hall effect in a light metal ti, *Nature* **619**, 52 (2023).
 - [2] M. Costa, B. Focassio, L. M. Canonico, T. P. Cysne, G. R. Schleder, R. B. Muniz, A. Fazzio, and T. G. Rappoport, Connecting higher-order topology with the orbital hall effect in monolayers of transition metal dichalcogenides, *Physical Review Letters* **130**, 116204 (2023).
 - [3] T. P. Cysne, M. Costa, L. M. Canonico, M. B. Nardelli, R. B. Muniz, and T. G. Rappoport, Disentangling orbital and valley hall effects in bilayers of transition metal dichalcogenides, *Physical Review Letters* **126**, 056601 (2021).
 - [4] D. Go, D. Jo, C. Kim, and H. W. Lee, Intrinsic spin and orbital hall effects from orbital texture, *Physical Review Letters* **121**, 086602 (2018).
 - [5] H. Kontani, T. Tanaka, D. S. Hirashima, K. Yamada, and J. Inoue, Giant orbital hall effect in transition metals: origin of large spin and anomalous hall effects, *Physical Review Letters* **102**, 016601 (2009).
 - [6] I. Baek and H.-W. Lee, Negative intrinsic orbital hall effect in group xiv materials, *Physical Review B* **104**, 245204 (2021).
 - [7] S. Bhowal and S. Satpathy, Intrinsic orbital and spin hall effects in monolayer transition metal dichalcogenides, *Physical Review B* **102**, 035409 (2020).
 - [8] S. Bhowal and S. Satpathy, Intrinsic orbital moment and prediction of a large orbital hall effect in two-dimensional transition metal dichalcogenides, *Physical Review B* **101**, 121112(R) (2020).
 - [9] D. Go, D. Jo, H.-W. Lee, M. Kläui, and Y. Mokrousov, Orbitronics: Orbital currents in solids, *EPL (Europhysics Letters)* **135**, 37001 (2021).
 - [10] M. Zeer, D. Go, J. P. Carbone, T. G. Saunderson, M. Redies, M. Kläui, J. Ghabboun, W. Wulfhekkel, S. Blügel, and Y. Mokrousov, Spin and orbital transport in rare-earth dichalcogenides: The case of eus_2 , *Physical Review Materials* **6**, 074004 (2022).
 - [11] D. Jo, D. Go, and H.-W. Lee, Gigantic intrinsic orbital hall effects in weakly spin-orbit coupled metals, *Physical Review B* **98**, 214405 (2018).
 - [12] L. Salemi and P. M. Oppeneer, Theory of magnetic spin and orbital hall and nernst effects in bulk ferromagnets, *Physical Review B* **106**, 024410 (2022).
 - [13] T. P. Cysne, S. Bhowal, G. Vignale, and T. G. Rappoport, Orbital hall effect in bilayer transition metal dichalcogenides: From the intra-atomic approximation to the bloch states orbital magnetic moment approach, *Physical Review B* **105**, 195421 (2022).
 - [14] R. S. Fishman, J. S. Gardner, and S. Okamoto, Orbital angular momentum of magnons in collinear magnets, *Physical Review Letters* **129**, 167202 (2022).
 - [15] D. Go, D. Jo, T. Gao, K. Ando, S. Blügel, H.-W. Lee, and Y. Mokrousov, Orbital rashba effect in a surface-oxidized cu film, *Physical Review B* **103**, L121113 (2021).
 - [16] S. Bhowal and G. Vignale, Orbital hall effect as an alternative to valley hall effect in gapped graphene, *Physical Review B* **103**, 195309 (2021).
 - [17] K. Das and A. Agarwal, Intrinsic hall conductivities induced by the orbital magnetic moment, *Physical Review B* **103**, 125432 (2021).
 - [18] R. R. Neumann, A. Mook, J. Henk, and I. Mertig, Orbital magnetic moment of magnons, *Physical Review Letters* **125**, 117209 (2020).
 - [19] P. Sahu, S. Bhowal, and S. Satpathy, Effect of the inversion symmetry breaking on the orbital hall effect: A

- model study, *Physical Review B* **103**, 085113 (2021).
- [20] L. M. Canonico, T. P. Cysne, A. Molina-Sanchez, R. B. Muniz, and T. G. Rappoport, Orbital hall insulating phase in transition metal dichalcogenide monolayers, *Physical Review B* **101**, 161409(R) (2020).
 - [21] L. Ponet and S. Artyukhin, First-principles theory of giant rashba-like spin splitting in bulk gete, *Physical Review B* **98**, 174102 (2018).
 - [22] T. P. Cysne, F. S. M. Guimarães, L. M. Canonico, M. Costa, T. G. Rappoport, and R. B. Muniz, Orbital magnetoelectric effect in nanoribbons of transition metal dichalcogenides, *Physical Review B* **107**, 115402 (2023).
 - [23] F. Xue, V. Amin, and P. M. Haney, Imaging the valley and orbital hall effect in monolayer mos_2 , *Physical Review B* **102**, 161103(R) (2020).
 - [24] D. Xiao, G. B. Liu, W. Feng, X. Xu, and W. Yao, Coupled spin and valley physics in monolayers of mos_2 and other group-vi dichalcogenides, *Physical Review Letters* **108**, 196802 (2012).
 - [25] D. Xiao, W. Yao, and Q. Niu, Valley-contrasting physics in graphene: magnetic moment and topological transport, *Physical Review Letters* **99**, 236809 (2007).
 - [26] V. Vargiamidis, P. Vasilopoulos, and N. Neophytou, Tunable topological phases in monolayer pt_2hgse_3 with exchange fields, *Physical Review B* **106**, 205416 (2022).
 - [27] X. Zou, H. Ma, R. Li, Y. Dai, B. Huang, and C. Niu, Gate-mediated transition between antiferromagnetic topological and chern insulators in honeycomb x_3mn_3 ($\text{x}=\text{sr},\text{ba}$), *Physical Review B* **106**, 075144 (2022).
 - [28] X. Feng, X. Xu, Z. He, R. Peng, Y. Dai, B. Huang, and Y. Ma, Valley-related multiple hall effect in monolayer vs_2p_4 , *Physical Review B* **104**, 075421 (2021).
 - [29] Z. He, R. Peng, Y. Dai, B. Huang, and Y. Ma, Single-layer sc_2 : A paradigm for valley-related multiple hall effect, *Applied Physics Letters* **119**, 243102 (2021).
 - [30] H. Hu, W.-Y. Tong, Y.-H. Shen, X. Wan, and C.-G. Duan, Concepts of the half-valley-metal and quantum anomalous valley hall effect, *Npj Computational Materials* **6**, 129 (2020).
 - [31] H. Huan, Y. Xue, B. Zhao, G. Gao, H. Bao, and Z. Yang, Strain-induced half-valley metals and topological phase transitions in mbr_2 monolayers ($\text{m}=\text{ru},\text{os}$), *Physical Review B* **104**, 165427 (2021).
 - [32] S. Li, Q. Wang, C. Zhang, P. Guo, and S. A. Yang, Correlation-driven topological and valley states in monolayer vs_2p_4 , *Physical Review B* **104**, 085149 (2021).
 - [33] W. Pan, Tuning the magnetic anisotropy and topological phase with electronic correlation in single-layer h-febr_2 , *Physical Review B* **106**, 125122 (2022).
 - [34] X. Zhou, R.-W. Zhang, Z. Zhang, W. Feng, Y. Mokrousov, and Y. Yao, Sign-reversible valley-dependent berry phase effects in 2d valley-half-semiconductors, *Npj Computational Materials* **7**, 160 (2021).
 - [35] W. Yao, D. Xiao, and Q. Niu, Valley-dependent optoelectronics from inversion symmetry breaking, *Physical Review B* **77**, 235406 (2008).
 - [36] X. Liu, A. P. Pyatakov, and W. Ren, Magnetoelectric coupling in multiferroic bilayer vs_2 , *Physical Review Letters* **125**, 247601 (2020).
 - [37] Y. Rouzhahong, C. Liang, C. Li, B. Wang, and H. Li, Valley piezoelectricity promoted by spin-orbit coupling in quantum materials, *Science China Physics, Mechanics & Astronomy* **66**, 247711 (2023).
 - [38] W. Y. Tong, S. J. Gong, X. Wan, and C. G. Duan, Concepts of ferrovalley material and anomalous valley hall effect, *Nature Communications* **7**, 13612 (2016).
 - [39] X. Wang, D. Li, Z. Li, C. Wu, C. M. Che, G. Chen, and X. Cui, Ferromagnetism in 2d vanadium diselenide, *ACS Nano* **15**, 16236 (2021).
 - [40] X. Li, T. Cao, Q. Niu, J. Shi, and J. Feng, Coupling the valley degree of freedom to antiferromagnetic order, *Proceedings of the National Academy of Sciences of the United States of America* **110**, 3738 (2013).
 - [41] G.-B. Liu, W.-Y. Shan, Y. Yao, W. Yao, and D. Xiao, Three-band tight-binding model for monolayers of group-vib transition metal dichalcogenides, *Physical Review B* **88**, 085433 (2013).
 - [42] J. Zhou, Q. Sun, and P. Jena, Valley-polarized quantum anomalous hall effect in ferrimagnetic honeycomb lattices, *Physical Review Letters* **119**, 046403 (2017).
 - [43] K. Zollner and J. Fabian, Engineering proximity exchange by twisting: Reversal of ferromagnetic and emergence of antiferromagnetic dirac bands in graphene/ $\text{cr}_2\text{ge}_2\text{te}_6$, *Physical Review Letters* **128**, 106401 (2022).
 - [44] Q. Cui, Y. Zhu, J. Liang, P. Cui, and H. Yang, Spin-valley coupling in a two-dimensional vs_2n_4 monolayer, *Physical Review B* **103**, 085421 (2021).
 - [45] T. Hu, F. Jia, G. Zhao, J. Wu, A. Stroppa, and W. Ren, Intrinsic and anisotropic rashba spin splitting in janus transition-metal dichalcogenide monolayers, *Physical Review B* **97**, 235404 (2018).
 - [46] C. Xu, J. Feng, M. Kawamura, Y. Yamaji, Y. Nahas, S. Prokhorenko, Y. Qi, H. Xiang, and L. Bellaiche, Possible kitaev quantum spin liquid state in 2d materials with $s = 3/2$, *Physical Review Letters* **124**, 087205 (2020).
 - [47] Z. Zhu and D. Tomanek, Semiconducting layered blue phosphorus: a computational study, *Physical Review Letters* **112**, 176802 (2014).
 - [48] See supplemental material xxx for calculation methods, fitting parameters, the orbital contribution, the spin contribution, wannier projection, and the orbital hall conductivity for different numbers of valence bands, which includes refs. [49–59], .
 - [49] G. Kresse and D. Joubert, From ultrasoft pseudopotentials to the projector augmented-wave method, *Physical Review B* **59**, 1758 (1999).
 - [50] G. Kresse and J. Furthmüller, Efficient iterative schemes for ab initio total-energy calculations using a plane-wave basis set, *Physical Review B* **54**, 11169 (1996).
 - [51] P. E. Blochl, Projector augmented-wave method, *Physical Review B* **50**, 17953 (1994).
 - [52] S. Grimme, J. Antony, S. Ehrlich, and H. Krieg, A consistent and accurate ab initio parametrization of density functional dispersion correction (DFT-D) for the 94 elements H-Pu, *The Journal of chemical physics* **132**, 154104 (2010).
 - [53] A. Rohrbach, J. Hafner, and G. Kresse, Electronic correlation effects in transition-metal sulfides, *Journal of Physics: Condensed Matter* **15**, 979 (2003).
 - [54] D. J. Thouless, M. Kohmoto, M. P. Nightingale, and M. denNijs, Quantized Hall Conductance in a Two-Dimensional Periodic Potential, *Physical Review Letters* **49**, 405 (1982).
 - [55] T. Jungwirth, Q. Niu, and A. H. MacDonald, Anomalous Hall effect in ferromagnetic semiconductors, *Physical Review B* **61**, 104404 (2000).

- view Letters **88**, 207208 (2002).
- [56] Y. Yao, L. Kleinman, A. H. MacDonald, J. Sinova, T. Jungwirth, D. S. Wang, E. Wang, and Q. Niu, First principles calculation of anomalous Hall conductivity in ferromagnetic bcc Fe, *Physical Review Letters* **92**, 037204 (2004).
 - [57] A. A. Mostofi, J. R. Yates, Y. S. Lee, I. Souza, D. Vanderbilt, and N. Marzari, wannier90: A tool for obtaining maximally-localised Wannier functions, *Computer Physics Communications* **178**, 685 (2008).
 - [58] X. Wang, J. R. Yates, I. Souza, and D. Vanderbilt, Ab initio calculation of the anomalous Hall conductivity by Wannier interpolation, *Physical Review B* **74**, 195118 (2006).
 - [59] Q. Wu, S. Zhang, H.-F. Song, M. Troyer, and A. A. Soluyanov, WannierTools: An open-source software package for novel topological materials, *Computer Physics Communications* **224**, 405 (2018).